Chapter II: Examples of Inversion of Refraction Data by Wavefield Continuation

Abstract

Two examples of the inversion of refraction data by downward continuation illustrate the applicability of the method to field data. The first example is a refraction profile from the Mojave Desert, California. The data are spatially aliased and there is clear evidence of lateral inhomogenities. The inversion in this case produces a broken image in the slowness-depth plane due to the lateral inhomogenity, but a useful average velocity model is still obtainable. The second example is a shallow marine reflection profile. Here, the truncation effects due to the finite horizontal aperature of the recording cable produce artifacts in the slowness-depth domain. The velocity model is, however distinct from the artifacts, and in this case, the presence of strong precritical reflections aids in the inversion.

2.1 Introduction

In Chapter I, a downward continuation method was presented for the inversion of densely recorded refraction data. This technique transforms the entire recorded data wavefield from the time-distance $(t-x)$ domain into the slowness-depth $(p-z)$ domain. The resulting velocity-depth locus is a focussed image in the $(p-z)$ domain, and the uncertainty in the solution is indicated by the width and coherence of this image. There are two basic assumptions in the procedure which limit its general applicability. The first is the assumption of lateral homogenity of the velocity function, and the second is the assumption that the data are sufficiently well sampled in the spatial dimension that they can be treated as a wavefield.

In this chapter we present two examples of the application of this method to real refraction data, which do not rigidly satisfy the assumptions mentioned above. The object is to illustrate the robustness and utility of the wavefield approach even when the data are not ideal. Two data sets are presented. The first profile is composed of vertical component velocity records from the Mojave Desert, and the second is a suite of acoustic responses recorded by a hydrophone cable in a shallow marine environment.

2.2 The Mojave Desert Profile

In the fall of 1980, the United States Geological Survey (USGS) conducted an extensive refraction project in the Mojave Desert of southern California. Only a portion of these data will be analysed here. The location of the profile we have chosen is shown in Figure 2.1, and the data traces are shown in Figure 2.2.

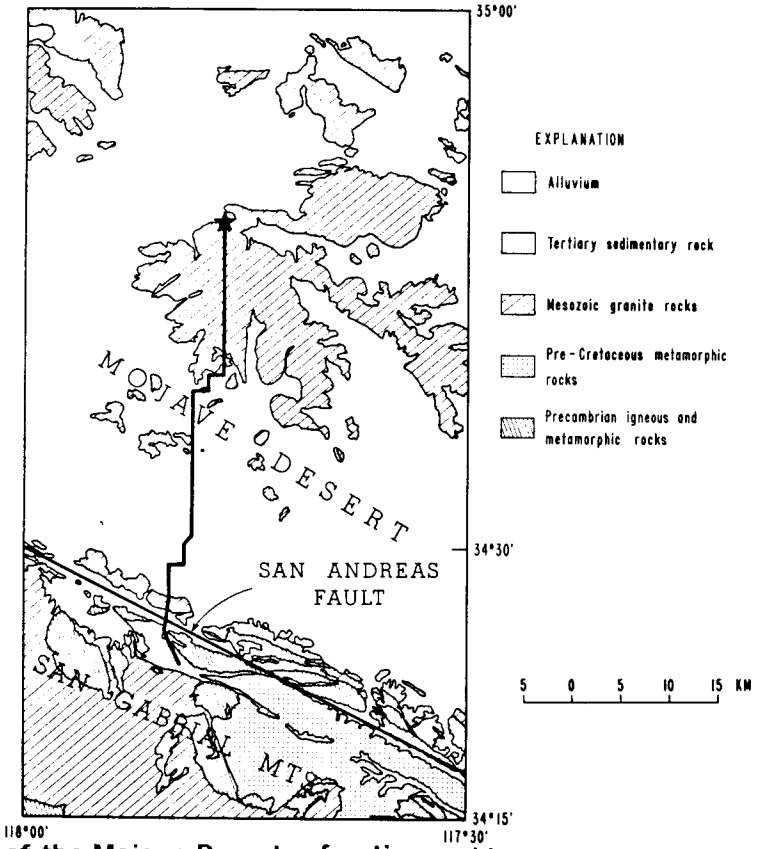

FIG. 2.1. Location of the Mojave Desert refraction profile. The seismograms recorded on this profile are shown in Figure 2.2.

A number of features are evident in the data (Figure 2.2). The first arrivals do not form a smooth locus of constantly decreasing slope (p), as would be observed if the Earth structure were laterally homogeneous. Most of these fluctuations can be attributed to surface pockets of sediments (G. Fuis, personal communication). Others, such as the early arrivals near x=37 km, are apparently related to changes of structure at faults (see Figure 2.1). These time anomalies do not prevent analysis of the data by wavefield transformation; but, as discussed below, they do contribute significantly to the uncertainty associated with the best fit laterally homogeneous model.

Figure 2.3 shows the slant stack of the data in Figure 2.2. A fairly coherent image can be seen traversing this wavefield in the (p,τ)-region from (0.188, 0.0) to (0.138,

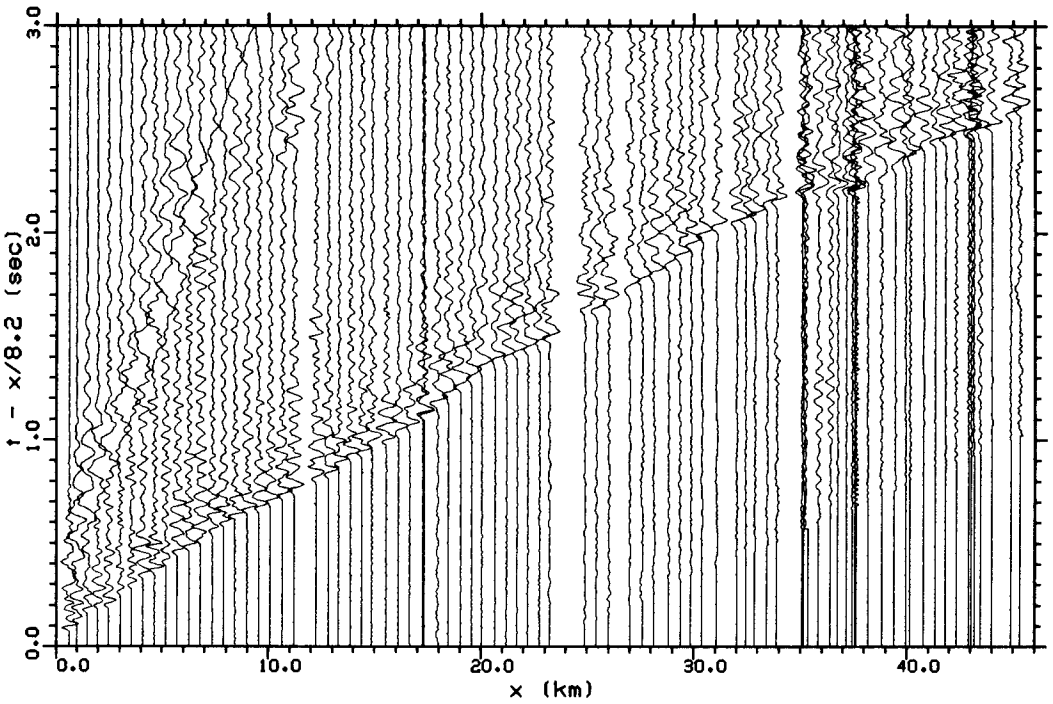

FIG. 2.2. Record section from the Mojave Desert data with a reduction velocity of 8.2 km/s. This profile is a composite of recordings of two shots, a smaller one recorded at x < 10 km and a larger one recorded at x > 10 km. The records are normalized so each has the same maximum amplitude.

1.6). The image does have some "en echelon" branches beside the main locus and some regions where τ is not monotonically decreasing that are due to the fluctuations in arrival times mentioned above. These anomalies are easier to see in Figure 2.4.

Iterative downward continuation of the $p-\tau$ wavefield in Figure 2.3 produces the slowness-depth image displayed in Figure 2.4. The solid line in Figure 2.4 is the velocity function at the final iteration and it coincides with the dominant image in the downward continued $(p-z)$ wavefield. However, because of the lateral variations in structure along the profile, the image is broken and sometimes multivalued. The convergence condition, as defined by the solid, monotonic velocity- depth curve can therefore be considered only as an average laterally homogeneous approximation to the velocity structure along the profile. The uncertainty in this representation of the structure, which is indicated by the width and incoherence of the image, is $\pm$0.8 km depth at all velocities less the 7 km/s. This uncertainty in depth can be attributed to a composite of two effects. First, the time resolution and frequency content in the original data is seen in the width of the individual branches of the split image, which accounts for about half the variation. The multiplicity of branches due to lateral velocity changes accounts for the remainder.

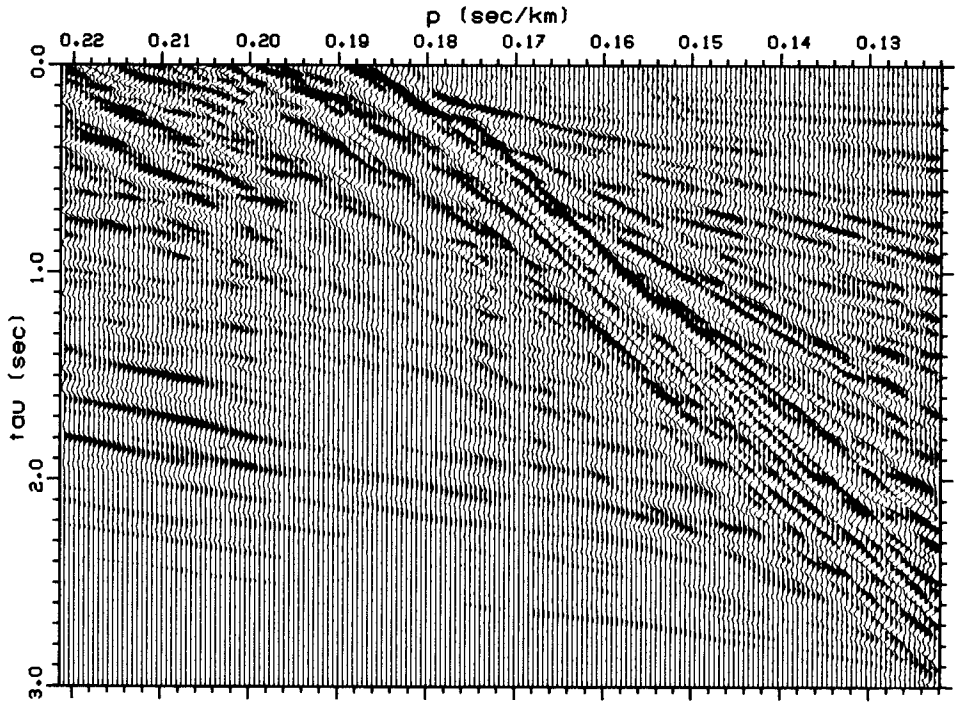

FIG. 2.3. Slant stack $(p-\tau)$ wavefield obtained by transformation of the Mojave Desert data in Figure 2.2. Iterative downward continuation of this wavefield produces the velocity-depth model.

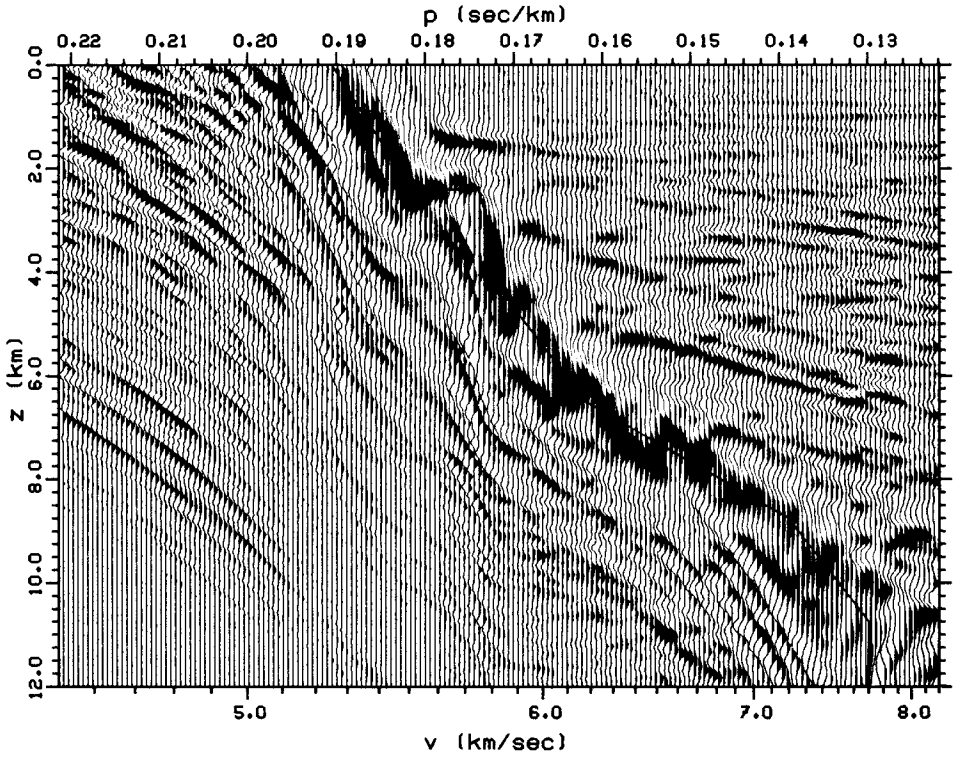

FIG. 2.4. The $(p-z)$ wavefield of the Mojave Desert data at convergence. The solid line superposed on the wavefield is the velocity depth model used in the final iteration in the downward continuation. The coincidence of the solid line and the image shows the convergence.

As a check on the adequacy of the model obtained, traveltimes were computed for the model by ray tracing. (Note that, up to this point, traveltimes have not been directly used to constrain the model.) The resulting time curve is superposed on the data in Figure 2.5. In general, the model produces a smooth curve that fits the first arrival observations to within 0.05 seconds. The fit is early at some distances and late at others, indicating that we have indeed obtained a reasonable average velocity structure by downward continuation.

Two triplications are evident in the traveltime curve in Figure 2.5. The one that occurs at 13 km $< x <$ 31 km is due to the rapid velocity increase near 2.3 km depth (Figure 2.4). This triplication may be real as there appears to be an increase in waveform complexity near the first arrivals over this distance range, which is consistent with the existence of a triplication. On the other hand, this feature may be an artifact introduced by fortuitous correlations across the variations in first arrival times due to lateral structure changes in this region. The latter interpretation is supported by the absence of the expected precritical reflection image in Figure 2.4. The precritical reflection would lie horizontal and touch the main image at the depth of the reflector (2.3 km). Examples of precritical reflections are shown in Figure 2.10 below.

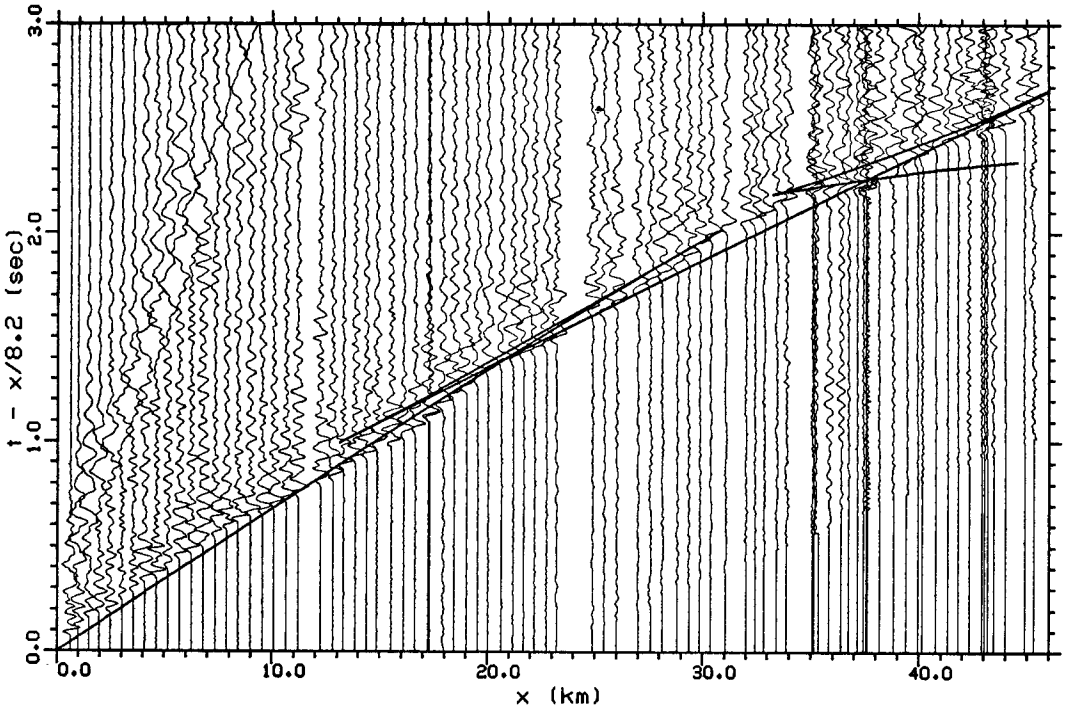

FIG. 2.5. Comparison of observed traveltimes and traveltimes computed from the velocity depth function shown as the solid line in Figure 2.4.

The second triplication lies at $x > 33$ km in Figure 2.5. This feature is clearly due to lateral rather than vertical velocity variations, as the highest velocity branch results from coherence of energy strongly affected by the San Andreas Fault (near x = 37 km). Consequently, the velocities in the model in Figure 2.4 are not reliable below 7 km depth.

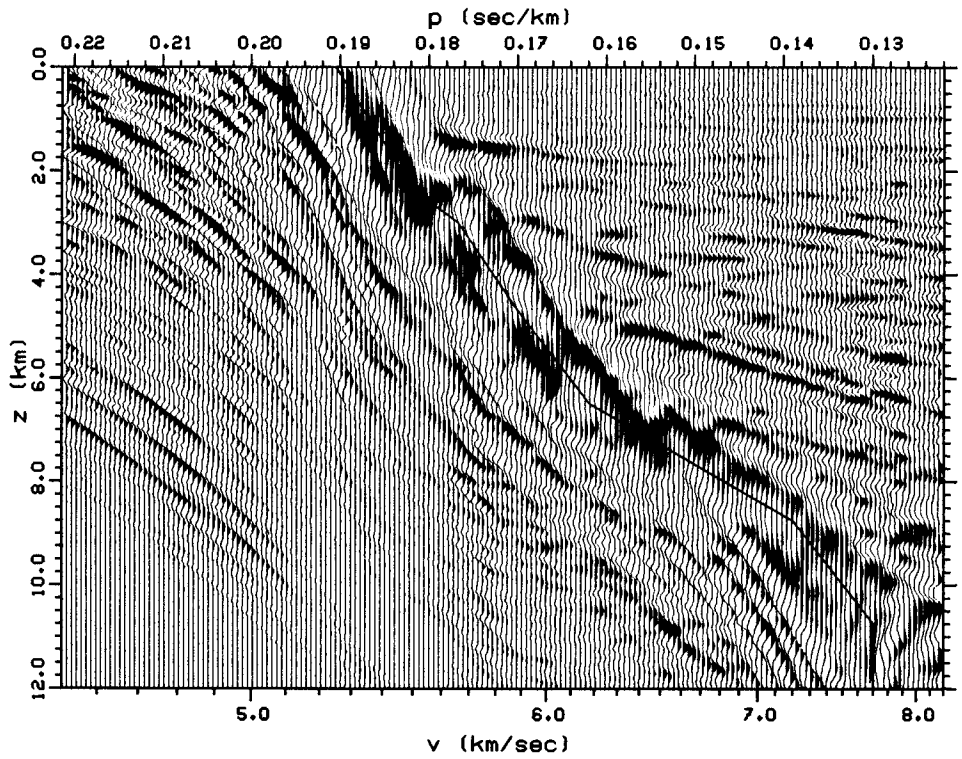

FIG. 2.6. An acceptable, but unconverged downward continuation solution. The solid line is a velocity-depth curve that produces acceptable traveltimes (see Figure 2.7) but does not correspond to stationarity of the $p-z$ wavefield.

In order to further investigate the stability of the solution in Figure 2.4, the model was altered to decrease the velocity gradient near 2.3 km depth. This model is shown as the solid line superposed on the wavefield obtained by downward continuation with it in Figure 2.6. This model does not give the wavefield stationarity required for convergence (note the shift of the wavefield in Figure 2.6 relative to that in Figure 2.4); however, as is shown in Figure 2.7, it fits the observed traveltimes as well as the convergent model does. To choose between the two models is difficult. The first model has converged, but this is a valid indication of a correct solution primarily for laterally homogeneous media. The second model fits the observed times adequately and is slightly simpler, but has not converged.

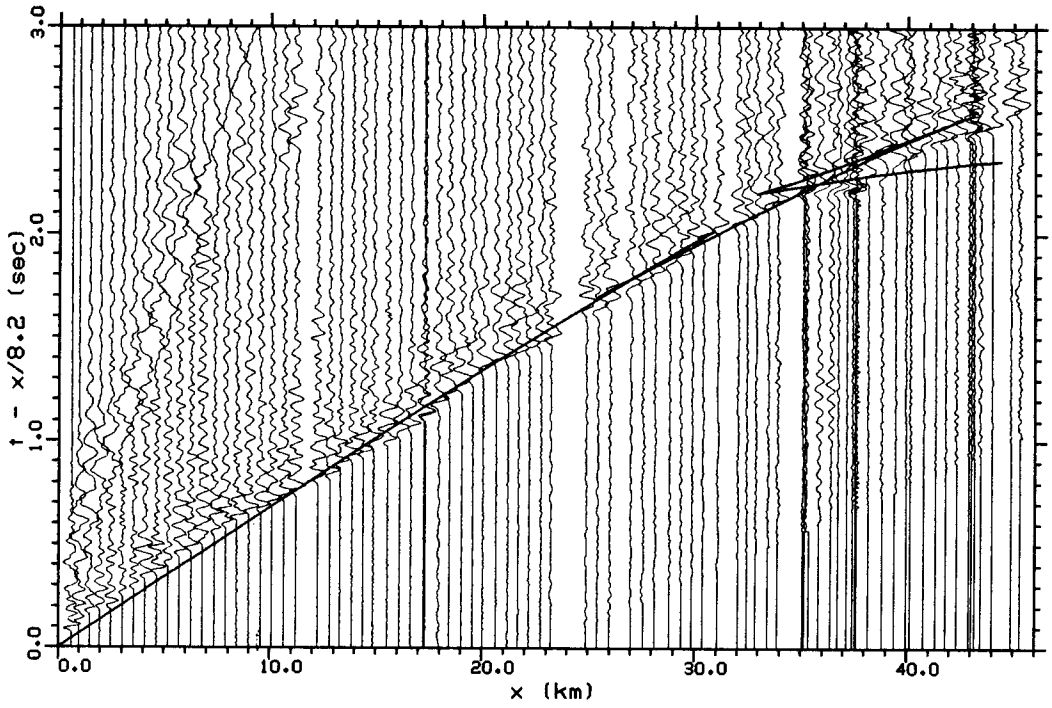

FIG. 2.7. Comparison of computed and observed traveltimes for the unconverged model in Figure 2.6. The predictions are shown as the solid line.

In summary, this analysis of the Mojave Desert data illustrates some of the trade-offs that occur when structure varies laterally. Specifically, a reasonable, average velocity-depth curve can be stably estimated, but the finer details of the curve may be related to lateral rather than vertical velocity variations. These effects are not confined to wavefield analysis, but the wavefield approach has the advantage of being relatively unbiased as the significance of any region of coherent energy in the data is not established until convergence is obtained. The identification of the possible triplication near 20 km is an example of this.

2.3 A Shallow Marine Profile

In a laterally homogeneous region, data in both the common-shot recording geometry, and the common midpoint interpretation coordinates used in seismic exploration can be directly inverted by wavefield transformation. In this section we present an example of the analysis of a common midpoint gather containing the acoustic response of the uppermost 1 km of sediments in a shallow marine environment. The data are shown in Figure 2.8.

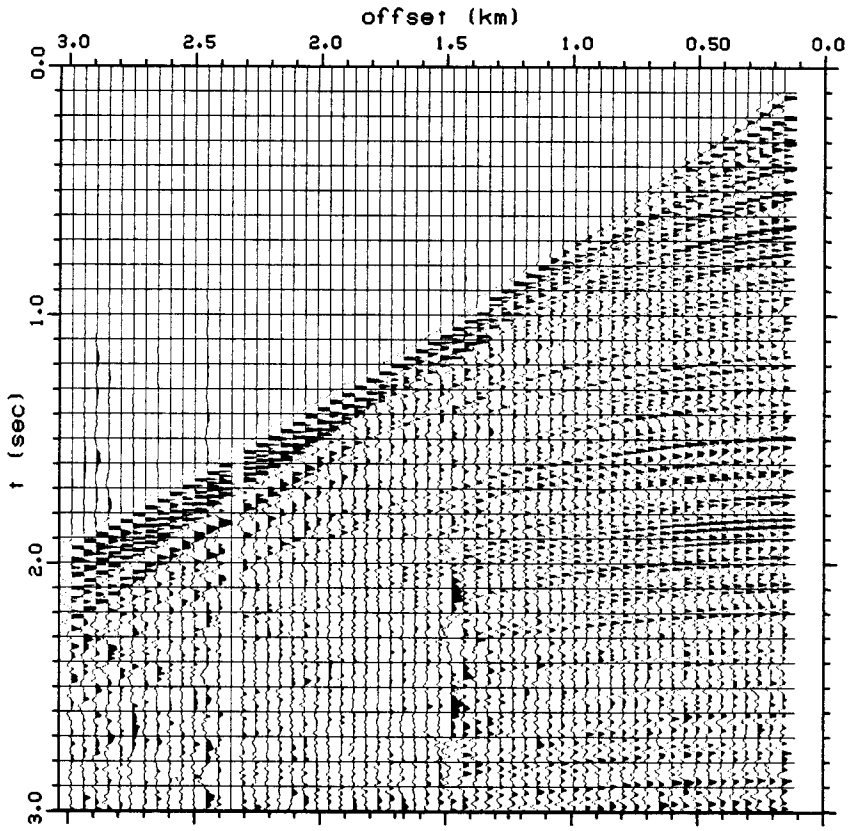

FIG. 2.8. Common mid-point marine profile. These data are plotted in the reflection seismology convention of time increasing downward (in contrast to the refraction format used for Figure 2.2). Since this is a common mid-point gather, we have plotted offset rather than shot distance.

Figure 2.9 shows the slant stack of the data in Figure 2.8. There are some artifacts visible in this wavefield; the most prominent ones (labelled T in Figure 2.9) are due to the truncation of the data at the two ends of the recording cable and appear as coherent straight lines. The $p-\tau$ image of interest consists of two sets of curves. The first is the main trajectory that lies in the (p,τ)-region from (0.69, 0.0) to (0.45, 0.6). The second type corresponds to pre-critical reflections which appear as hyperbolic trajectories in the upper right part of Figure 2.9 (labelled A and B).

The existence of strong pre-critical reflection images in these marine data provides useful constraints on the iterative convergence of the downward continuation of the $p-\tau$ wavefield to produce the model (solid line in Figure 2.10). When the correct velocity profile is used, pre-critical reflections produce a straight, horizontal image in the $p-z$ plane at the depth of the reflector. The image is horizontal because all the p values assosicated with the reflection event bottom at the same depth. The uppermost reflection (A) in Figure 2.10 is from the water-sediment interface. The image is poorly

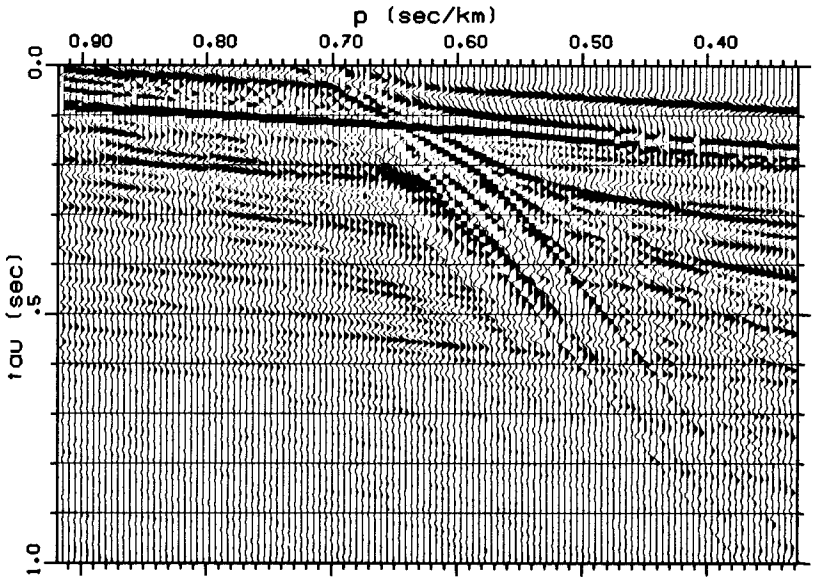

FIG. 2.9. Slant stack ($p-\tau$) wavefield obtained by transformation of the marine data in Figure 2.8. Iterative downward continuation of this $p-\tau$ wavefield produces convergence with the velocity profile and $p-z$ wavefield in Figure 2.10. The curves labelled A through D are precritical reflections. The curve labelled T is a cable truncation artifact.

defined between (A) and the inter-sediment reflection (B). The RMS velocity is, however, apparently correct because image (B) is straight and horizontal. The clearest part of the image is from 0.5 to 1.0 km depth where there is a coherent trajectory indicating a nearly linear increase of velocity with depth. Such an increase is consistent with the observation of a gently curved first arrival branch in the traveltime curve between the 1.5 and 3.0 km offsets in Figure 2.8.

In order to check the overall behavior of the model in Figure 2.10, the traveltimes corresponding to this model were computed and superposed on the data as shown in Figure 2.11. In addition the reflections from the two velocity steps mentioned above, potential reflection times from the high velocity gradient near 0.45 km-depth (labelled C), and the mild gradient near 0.80 km-depth (labelled D) are also shown. All four reflections appear to be expressed in the data, particularly at the near offsets. Evidence for additional small velocity steps is seen in the traveltime and $p-z$ domains. We have not attempted to image them all.

One of the advantages of the wavefield transformation approach is that no preprocessing of the data was required. The complete data sets were used in raw form, so the final images contain no arbitrary selection of data. For analysis of large scale refraction profiles, such as the Mojave data, wavefield transformation produces a solution in a matter of hours. For exploration (reflection) oriented processing, wavefield

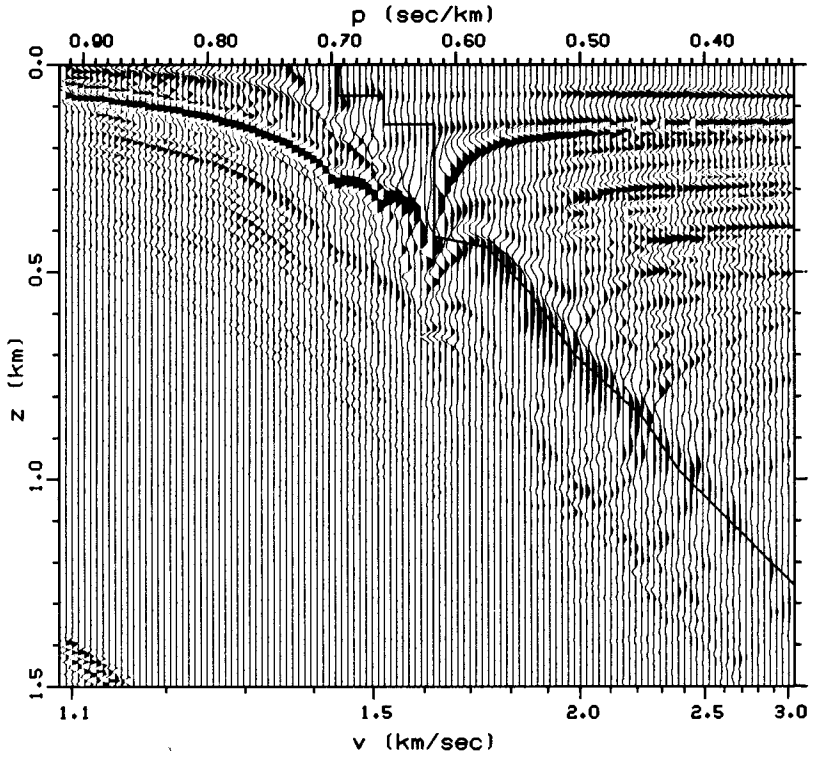

FIG. 2.10. The $p-z$ wavefield of the marine data profile at convergence. The solid line superposed on the wavefield is the velocity-depth used in the downward continuation.

transformation of refractions provides a method of extracting independent velocity information from a portion of the wavefield that has previously been neglected by conventional analyses.

Conclusions

The method of refraction inversion by wavefield transformation has been illustrated by application to two rather different data sets, one recorded on land in a large scale common-shot refraction geometry, and the other recorded in a shallow marine environment with a standard acoustic exploration cable. In both cases, the results obtained are compatible with those of conventional processing. Wavefield transformation is seen to be robust, unbiased, and particularly suited to processing large volumes of data. These features, combined with the conceptual elegance involved in forming the solution from the data itself, encourage further development and application of the method.

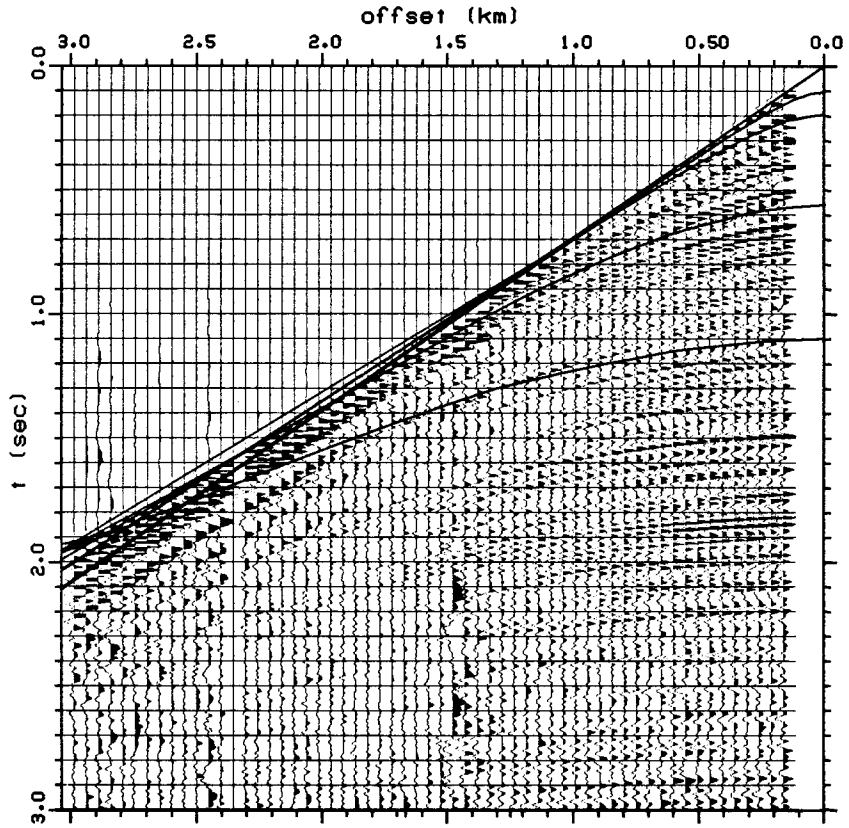

FIG. 2.11. Comparison of observed and predicted traveltimes. The solid lines superposed on the data are times predicted by the model in Figure 2.10. The precritical reflections labelled A through D correspond to those shown in Figures 2.9 and 2.10.